Confirmation of ferroelectricity, piezoelectricity, and crystal structure of the electronic dielectric $TmFe_2O_4$

Shinya Konishi,[1,*] Daisuke Urushihara,[2,*] Tatsuya Hayakawa,[2] Koichiro Fukuda,[2] Toru Asaka,[2,3] Koji Ishii,[4] Noriaki Naoda,[1] Mari Okada,[1] Hirofumi Akamatsu,[5] Hajime Hojo,[6] Masaki Azuma,[7] and Katsuhisa Tanaka[1,†]

[1]*Department of Material Chemistry, Graduate School of Engineering, Kyoto University, Katsura, Nishikyo-ku, Kyoto 615-8510, Japan*

[2]*Division of Advanced Ceramics, Nagoya Institute of Technology, Showa-ku, Nagoya 466-8555, Japan*

[3]*Frontier Research Institute for Materials Science (FRIMS), Nagoya Institute of Technology, Showa-ku, Nagoya 466-8555, Japan*

[4]*Asylum Research, Oxford Instruments KK, Shinagawa-ku, Tokyo 140-0002, Japan*

[5]*Department of Applied Chemistry, Faculty of Engineering, Kyushu University, Motooka 744, Fukuoka 819-0395, Japan*

[6]*Department of Advanced Materials Science and Engineering, Faculty of Engineering Science, Kyushu University, Kasuga-shi, Fukuoka 816-8580, Japan*

[7]*Laboratory for Materials and Structures, Institute for Innovative Research, Tokyo Institute of Technology, Midori-ku, Yokohama 226-8503, Japan*

(Received 17 December 2021; revised 30 October 2022; accepted 30 November 2022; published 12 July 2023)

A charge order-driven ferroelectricity, a novel mechanism completely different from conventional types such as lattice distortion observed in a typical ferroelectric, has been expected for a series of compounds RFe_2O_4 (R = Ho ~ Lu and Y, In), but a real problem has been still unsolved whether or not the compounds are truly ferroelectric. Here, we demonstrate that $TmFe_2O_4$, one of the RFe_2O_4 family, is a true ferroelectric and piezoelectric compound with noncentrosymmetric structure (space group: Cm) at room temperature by using switching spectroscopy piezoelectric force microscopy, laser interferometry, scanning nonlinear dielectric microscopy, x-ray diffraction, selected-area electron diffraction, nano-beam electron diffraction, convergent-beam electron diffraction, and high-angle annular dark-field scanning transmission electron microscopy for single-crystalline $TmFe_2O_4$. We have also found that $TmFe_2O_4$ exhibits an electric field induced phase transition between ferroelectric and conductive states. We propose that the charge ordering of Fe^{2+} and Fe^{3+} ions accompanied by an ordered displacement of Tm^{3+} ions lead to the ferroelectricity and piezoelectricity.

DOI: 10.1103/PhysRevB.108.014105

I. INTRODUCTION

Ferroelectrics are important materials extensively utilized as a sensor, a capacitor, an actuator, and so forth. As for the mechanism of ferroelectricity, a displacive type found in $BaTiO_3$, a prototype of ferroelectric, is very common. A hybrid improper type, another mechanism of ferroelectricity, has attracted much attention recently [1–11]. A charge order driven ferroelectricity, completely different from those two mechanisms, has been proposed for RFe_2O_4 (R = Ho ~ Lu and Y, In). From such a point of view, RFe_2O_4 is called an electronic dielectric. The compounds comprise two adjacent Fe layers, where the Fe ions form a planar triangular lattice. One conceivable arrangement of equal numbers of Fe^{3+} and Fe^{2+} ions occupying the triangular lattice is that one layer contains excess Fe^{3+} and the other excess Fe^{2+}. Such an arrangement can generate electric dipoles between the two adjacent layers and the dipoles can induce ferroelectricity. In 2005, Ikeda *et al.* [12] found that a pyroelectric current, the direction of which could be switched by an external electric field, flowed in single-crystalline $LuFe_2O_4$, leading to the conclusion that $LuFe_2O_4$ exhibits room-temperature ferroelectricity due to the charge ordering among Fe ions. In contrast, some reports deny the ferroelectricity of RFe_2O_4. X-ray scattering measurements by de Groot *et al.* [13] on single-crystalline $LuFe_2O_4$ indicate that the dielectric ground state of $LuFe_2O_4$ is antiferroelectric. Also, attempts were made to obtain a polarization-electric field hysteresis loop to prove the ferroelectricity via macroscopic techniques [14–17], but they resulted in failure. This is mainly because RFe_2O_4 shows rather high electrical conductivity, and it is hard to avoid a leakage current during the measurements of dielectric polarization.

Thus, an issue as to whether the RFe_2O_4 is ferroelectric or not remains unsolved. In the present study, we clarify the crystal structure as well as dielectric properties of single-crystalline $TmFe_2O_4$, one of the RFe_2O_4 family, to find an answer to this not yet settled question. A choice of $TmFe_2O_4$ comes from the fact that there are few data about structure and properties of $TmFe_2O_4$ reported thus far [18,19]. This is partly because single-crystalline $TmFe_2O_4$ is less easily prepared when compared with $LuFe_2O_4$; it is thought that the RFe_2O_4 phase becomes more unstable with a larger R^{3+} ion because R^{3+} must occupy an oxygen octahedral site which is too small for a larger cation. In addition, as described above, the dielectric ground state of $LuFe_2O_4$ still remains

*These authors contributed equally to this work.
†Corresponding author: tanaka@dipole7.kuic.kyoto-u.ac.jp

unclear, but RFe$_2$O$_4$ phases other than LuFe$_2$O$_4$ may give us unambiguous answer to this controversial issue. Our detailed structural analysis employed in the present work demonstrates that the room-temperature structure of TmFe$_2$O$_4$ is noncentrosymmetric. As for the dielectric properties, we have utilized switching spectroscopy piezoelectric force microscopy (SS-PFM) and scanning nonlinear dielectric microscopy (SNDM). Yang *et al.* [20] performed electrostatic force microscopy (EFM) and PFM on single-crystalline LuFe$_2$O$_4$ and found that the dielectric domain structure was observed in the EFM image but never by the PFM. They concluded that LuFe$_2$O$_4$ was not piezoelectric but ferroelectric with electronic origin. In this study, however, we verify that TmFe$_2$O$_4$ is both ferroelectric and piezoelectric at room temperature. We also quantitatively determine the piezoelectric coefficient by using laser interferometry. To corroborate the experimental results, first-principles calculations were performed to verify whether polar or non-polar structure of TmFe$_2$O$_4$ is more stable (see the Supplemental Material [21].

II. EXPERIMENTAL

A single-crystalline TmFe$_2$O$_4$ was grown by a floating zone melting method. The crystallinity, defined as a linewidth at half maximum of rocking curve of x-ray diffraction, was 0.024° [36], suggesting that we obtained a high crystallinity sample, although the present sample contains oxygen vacancy as clarified by our previous measurements using the thermogravimetry [36]. The composition was estimated to be TmFe$_2$O$_{3.93}$. The nonstoichiometry was reflected in the spin glass transition observed for the sample [37]. However, for convenience, we express the composition as TmFe$_2$O$_4$ in the text. The relationship of crystallographic axes between the paraelectric and ferroelectric phases is illustrated, as shown in Figs. S4(c) and S4(d) of the Supplemental Material, which will be described later, where the two sets of crystallographic axes (a_h, b_h, c_h) and (a_m, b_m, c_m) are for the hexagonal and monoclinic systems, respectively.

The ferroelectric and piezoelectric properties were measured by using SS-PFM (Oxford Instruments, MFP-3D Classic). The single crystal obtained by the floating zone melting method was cleaved so that the surface was the C_h plane, and the plate-like sample with their surfaces being the C_h plane was fabricated by polishing the cleaved surfaces. We also prepared a plate-like sample the surface of which was parallel to the c_h axis (perpendicular to the C_h plane) by cutting the single-crystalline TmFe$_2$O$_4$. For these samples, one of the surfaces was coated with silver paste and attached to a flat electrode made of stainless steel in the measurement system. The thickness of these samples is 1 mm. A cantilever, the resonance frequency of which was 305 kHz, was contacted to one surface of the sample, and both ac and dc voltages were applied by following the method proposed by Jesse *et al.* [38]. The dc voltage was varied within a range of ±8.5 V. The ac voltage, whose magnitude and frequency were 1.5 V and 305 kHz, respectively, was simultaneously applied to detect the direction or phase of the polarization generated by the dc voltage. At the same time, the displacement of the cantilever, which involved the strain of the sample and varied depending on the dc voltage, was evaluated by measuring the intensity of laser that was incident on and reflected from the cantilever. We measured the phase of polarization and the displacement while the dc voltage was kept constant. Also, we carried out similar measurements after turning off the dc electric field to evaluate the residual polarization. The measurements were performed at 303 to 363 K. Here, it should be noted that the frequency of the ac electric field is coincident with the resonant frequency of the cantilever in the present system, which enables us to obtain efficiently data with high signal-to-noise ratio. Also, the present SS-PFM machine possesses the ability of tracking so that the resonance state can be quickly recovered even if the phase of vibration of the cantilever becomes out of the resonance due to the roughness of the sample surface. It is considered that the electric field is not uniform inside the bulk TmFe$_2$O$_4$ sample in the SS-PFM measurements because one of the two electrodes is a stainless steel plate but the other is a tip which has point contact with the surface of the single-crystalline sample. The distribution of the electric field applied to TmFe$_2$O$_4$ was evaluated by using the finite element analysis (see Fig. S2 in the Supplemental Material). The inversion of the spontaneous polarization parallel to the c_h axis of TmFe$_2$O$_4$ was also verified by SNDM (Hitachi High-tech Corporation).

The piezoelectric coefficient was measured at 303 K by using laser interferometry (aixACCT Systems GmbH, aixD-BLI) for the single-crystalline sample of TmFe$_2$O$_4$ with the surface being perpendicular to the c_h axis. Au thin films were deposited on both sides of the single-crystalline sample as an electrode. The laser's luminance undergoes changes because the optical path length changes due to the piezoelectric response. The change of luminance based on the change of the thickness caused by the external dc electric field applied perpendicular to the sample surface, i.e., parallel to the c_h axis was explored. Similar measurements were carried out for α-quartz as a reference and the piezoelectric coefficient of the TmFe$_2$O$_4$ was calculated from the laser's luminance and thickness values of α-quartz. The capacitance and the dielectric loss were measured at 303 K by using an LCR (inductance – capacitance – resistance) meter equipped with the laser interferometry system. For the measurements, dc and ac electric fields were simultaneously applied parallel to the c_h axis of single-crystalline TmFe$_2$O$_4$. The magnitude and the frequency of ac electric field were set to 1 V and 1 kHz, respectively. The capacitance and the dielectric loss were evaluated as a function of dc electric field.

The x-ray diffraction (XRD) data were collected using a single crystal x-ray diffractometer, D8 VENTURE (Bruker) equipped with complementary metal-oxide-semiconductor (CMOS) detector and Mo $K\alpha$ x-ray tube (50 kV, 1 mA). A piece of single crystal was shaped sphere and mounted on a borosilicate glass rod. Lattice constants were determined using the program SAINT [39] and multi-scan absorption correction was carried out by using the program SADABS [39]. The initial structure model was calculated using the program Superflip based on the charge-flipping algorithm [40]. The crystal structure analysis was carried out using the software JANA2006 program package [41], and the crystal structure thus obtained was visualized by the VESTA program [42]. A thin sample for transmission electron microscopy was obtained by the conventional Ar^+ ion milling technique.

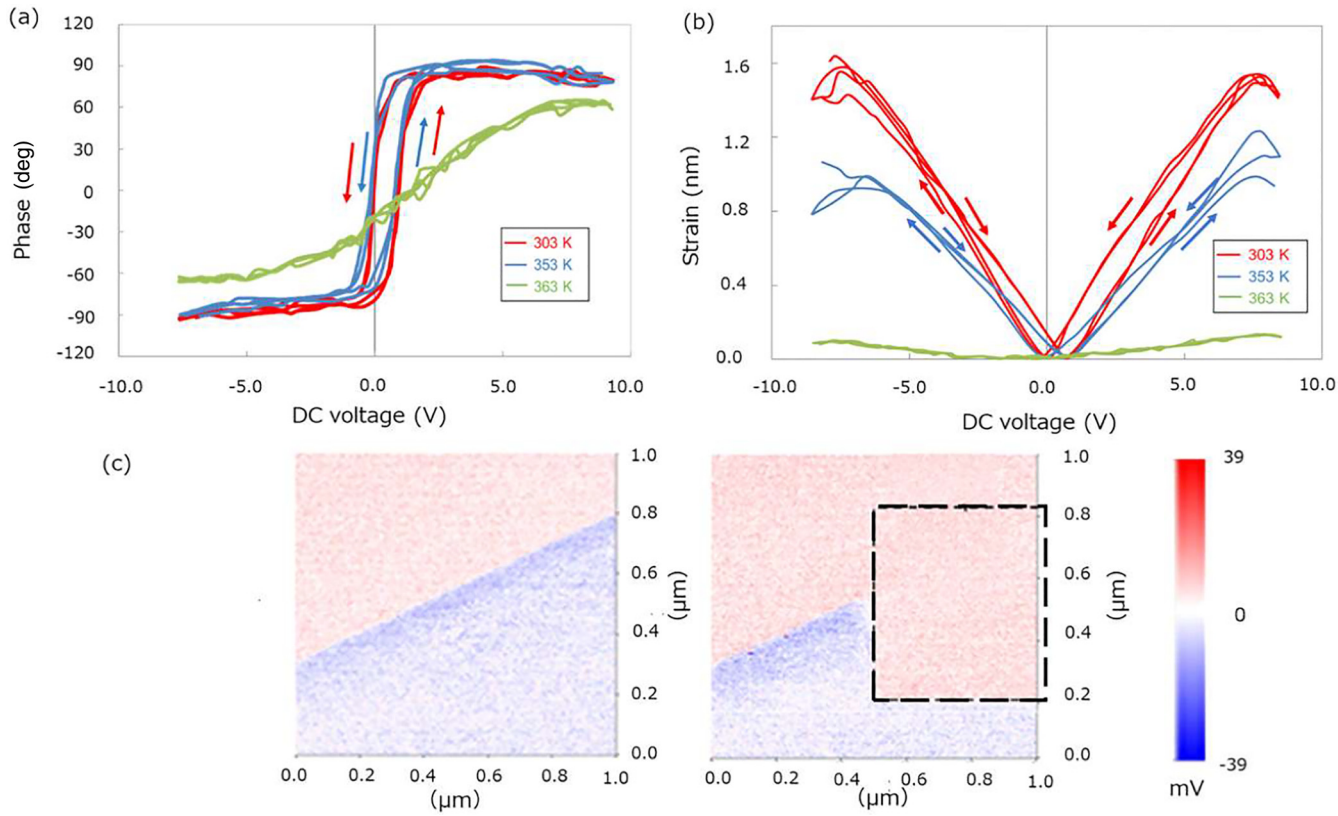

FIG. 1. Ferroelectricity and piezoelectricity in $TmFe_2O_4$. dc voltage dependence of (a) phase of polarization and (b) strain along the c_h axis of $TmFe_2O_4$ as a function of temperature obtained by applying the dc electric field parallel to the c_h axis of $TmFe_2O_4$. (c) Inversion of spontaneous polarization along the c_h axis of $TmFe_2O_4$ demonstrated by SNDM measurements at 303 K. The left and right figures show the domain structures before and after the application of dc voltage of 10 V parallel to the c_h axis in the area surrounded by the dotted lines (right figure). The red and blue regions represent the domains where the directions of the spontaneous polarizations are opposite to each other.

The selected-area electron diffraction (SAED) patterns and dark-field images were observed with JEM-2010HR (JEOL), operated at 200 kV. Moreover, nano-beam electron diffraction (NBED) and convergent-beam electron diffraction (CBED) measurements were carried out to obtain the local structural symmetry by using JEM-ARM200F (JEOL), operated at 200 and 80 kV, respectively. High-angle annular dark-field (HAADF)-scanning transmission electron microscopy (STEM) was used for direct observation of the crystal structure, operated with JEM-ARM200F (JEOL) at 200 kV. The HAADF-STEM image was processed by the image processing software DeConvHAADF (HREM Research Inc.) [43], which enables deconvolution of a raw STEM image with a probe function.

III. RESULTS AND DISCUSSION

The SS-PFM measurements were carried out to evaluate the direction of polarization and the strain induced by external dc electric field in the single-crystalline $TmFe_2O_4$. Figures 1(a) and 1(b) show, respectively, the phase of polarization and the displacement of the cantilever, the latter of which corresponds to the strain along the c_h axis induced in $TmFe_2O_4$ at varied temperatures from 303 to 363 K. The dc voltage was applied parallel to the c_h axis of $TmFe_2O_4$ in this case. A hysteresis loop is unambiguously observed at 303 K in both figures. Figures S1(a) and S1(b) indicate the existence of residual polarization at 303 K, when the dc voltage is off. Also, the phase of polarization is almost saturated at around a voltage of ± 2 V, and the phase of saturation polarization at $+2$ V differs by about 180° from that at -2 V. The difference in phase of saturation polarization suggests that the direction of dielectric polarization can be reversed by the external electric field. The inversion of the spontaneous polarization parallel to the c_h axis of $TmFe_2O_4$ was also verified by SNDM, as shown in Fig. 1(c). The initial state of polarization is illustrated in the left figure. The red and blue regions are domains containing spontaneous polarizations along the c_h axis, the directions of which are opposite to each other. The right figure is the domain structure after a dc voltage of 10 V is applied to the area surrounded by the dotted lines. It is found that the polarization is reversed by the external field as indicated by the change in color. This fact clearly suggests that $TmFe_2O_4$ is ferroelectric at 303 K. It is also seen from Figs. 1(a) and 1(b) that both hysteresis loops become unclear as the temperature is increased and eventually disappear at 363 K, indicating that $TmFe_2O_4$ undergoes a transition from ferroelectric to paraelectric states at around this temperature. In particular, the dc voltage dependence of strain exhibits parabolic behavior at 363 K. This indicates that the electrostrictive effect emerges in the paraelectric phase [Figs. S1(c) and S1(d)]. Here, it should be noted that the

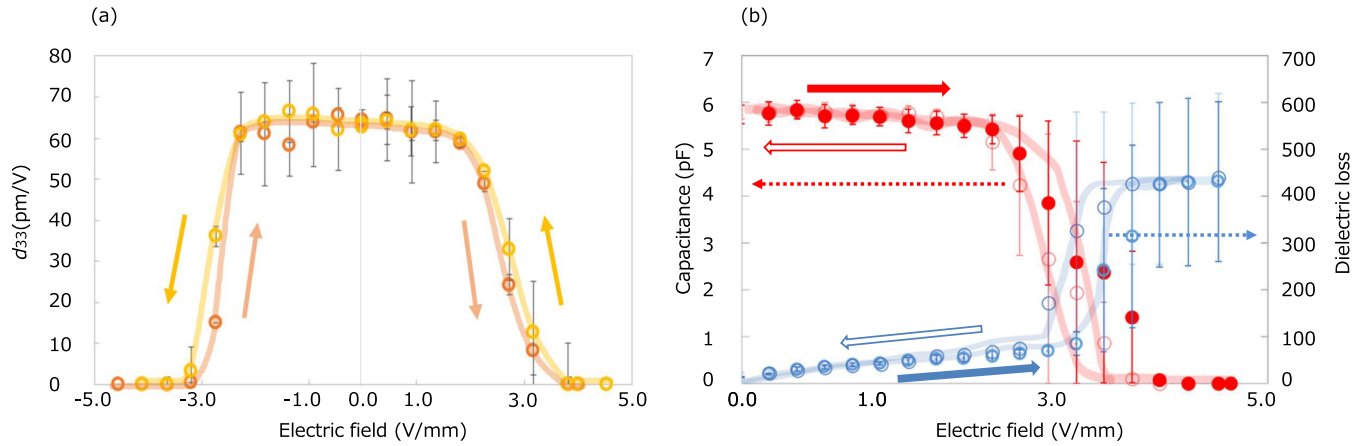

FIG. 2. Evaluation of the dielectric properties in $TmFe_2O_4$. (a) dc electric field dependence of piezoelectric coefficient, d_{33}, a component corresponding to a strain along the c_h axis with a dc electric field parallel to the c_h axis of $TmFe_2O_4$. (b) dc electric field dependence of capacitance and dielectric loss at 303 K. The electric field was applied parallel to the c_h axis.

hysteresis loop observed in SS-PFM measurements sometimes has an origin different than the ferroelectricity [44]. Nonetheless, the results of SNDM measurements as well as the hysteresis loop shown in Fig. 1(a) clearly confirm that $TmFe_2O_4$ is ferroelectric at room temperature.

It should be noted that the SS-PFM is not suitable for the quantitative estimation of the piezoelectric coefficient. Since the size of the tip of the cantilever is much smaller than the metallic plate electrode in the present case, the electric field is not homogeneous especially at around the surface of the material with which the tip is in contact [Figs. S2(a) and S2(b)]. In other words, an accurate value of electric field cannot be evaluated from the applied voltage and the sample thickness. Thus, we quantitatively determined the piezoelectric coefficient of $TmFe_2O_4$ by using the laser interferometry instead of the SS-PFM. Figure 2(a) depicts the dc electric field dependence of the piezoelectric coefficient d_{33}, a component corresponding to a strain along the c_h axis of $TmFe_2O_4$ caused by a dc electric field applied parallel to the c_h axis. The voltage was varied in a range -4.5 to 4.5 V, and the piezoelectric coefficient was determined at each voltage. The same measurements were performed for α quartz as a reference material, the piezoelectric coefficient of which was used to evaluate the value of d_{33} for $TmFe_2O_4$. Figure 2(a) indicates that the piezoelectric coefficient is almost independent of the electric field in a range -2.5 to $+2.5\,\mathrm{V\,mm^{-1}}$, whereas it rapidly decreases as the strength of electric field exceeds about $2.5\,\mathrm{V\,mm^{-1}}$. The constant value of piezoelectric coefficient is $64\,\mathrm{pm\,V^{-1}}$. The rapid decrease in the piezoelectric coefficient as the strength of electric field is intensified suggests that the charge ordered state of Fe^{3+} and Fe^{2+} ions collapses and the electronic structure is converted from ferroelectric to conductive states by the application of intense electric field. Also, this conversion reversibly takes place. A similar phenomenon, that is, a reversible conversion between insulating and conductive states depending on the external electric field, was reported for single crystal, polycrystal, and thin film of $LuFe_2O_4$ [45–48]. Cao *et al.* [48] confirmed that an intrinsic current-driven resistivity switching takes place at room temperature, although the additional Joule heating effect contributes to the change in temperature dependence of resistivity as well when the electric field exceeds a critical value at which an abrupt increase of current density is observed. It is reasonable to conclude that a similar intrinsic electric field driven transition between ferroelectric and conductive states occurs for the single-crystalline $TmFe_2O_4$, although additional effect of Joule heat cannot be thoroughly ruled out at this moment.

Figure 2(b) depicts the capacitance and the dielectric loss as a function of dc electric field at 303 K. The measurements were carried out by using an LCR meter equipped with the laser interferometry system while applying both dc and ac fields parallel to the c_h axis. The amplitude and the frequency of ac voltage are 1 V and 1 kHz, respectively. It is clearly found that the capacity drastically decreases as the dc electric field is above 3–4V $\mathrm{mm^{-1}}$, and accordingly, a rapid increase in the dielectric loss is observed around the same electric field. This change is reversible, similarly to the dc electric field dependence of piezoelectric coefficient as shown in Fig. 2(a). Thus we have demonstrated that the ferroelectricity is closely related to the charge ordering in RFe_2O_4.

The room-temperature structure was refined by single-crystal XRD data [Figs. S3(a)–S3(h) and S4(a)–S4(d)], based on the noncentrosymmetric space group Cm. To determine the superstructure unit cell for a structure analysis using XRD data, we performed NBED, as well as XRD precession images. The diffraction spots in NBED patterns were represented as threefold superstructure reflections with the modulation wave vector of $\boldsymbol{q} = (1/3)\boldsymbol{b}^*$ in the monoclinic basis [Figs. S3(c) and S3(d)]. In the XRD patterns, the superstructure reflections were particularly strong at the position of $0\,k/3\,l/3$ rather than that of $0\,k/3\,l/6$ in the diffuse streaks [Figs. S3(a) and S3(b)]. This indicates that the modulation wave vector is essentially not $\boldsymbol{q} = (1/3)\boldsymbol{b}^* + (1/2)\boldsymbol{c}^*$, but $\boldsymbol{q} = (1/3)\boldsymbol{b}^*$. Considering these comprehensively, the superstructure unit cell of $TmFe_2O_4$ was determined to be monoclinic with the lattice parameters of $a = 6.0269(2)$ Å, $b = 10.4388(3)$ Å, $c = 8.5898(3)$ Å and $\beta = 103.534\,(2)^\circ$. Figure 3(a) depicts the bright field pattern (BP) of CBED. Since CBED patterns contain the dynamical diffraction effects, we can obtain detailed crystallographic information such as a point group and presence of inversion symmetry. By analyzing [001]-zone whole pattern (WP), ± dark field patterns (DPs),

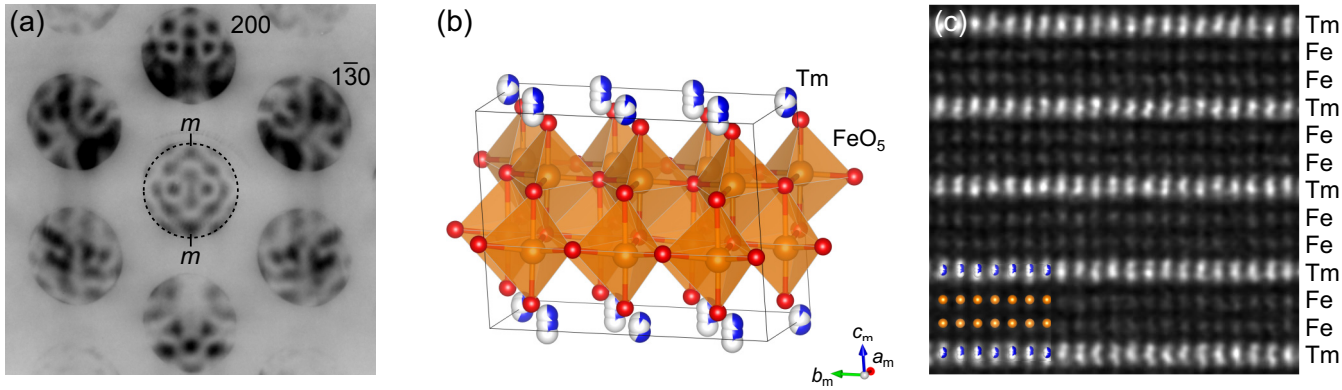

FIG. 3. Crystal structure of $TmFe_2O_4$. (a) [001]-zone axis bright-field pattern of CBED. (b) Crystal structure model for the ferroelectric phase of $TmFe_2O_4$. (c) [100]-zone HAADF-STEM image. Inset shows the crystal structure refined by using single crystal XRD data.

as well as BP, we determined that the point group is m [Figs. S3(e)–S3(h)]. From the point group and extinction rules obtained by CBED and XRD patterns, we uniquely determined that the space group is Cm [Figs. S3(e)–S3(h)]. We integrated the diffraction intensity based on the above-mentioned unit cell by optimizing the region to obtain only intensity of integer reflections and refined the crystal structure, taking account of a rotational twin structure with six twin variants. The twin structure must be formed due to breaking of threefold and inversion symmetries during the structural phase transition from trigonal $R\bar{3}m$ to monoclinic Cm [Figs. S4(a) and S4(b)]. The twin fractions obtained by the analysis were approximately one-sixth: 0.18(3), 0.150(12), 0.158(12), 0.159(11), 0.171(12), and 0.182(12). A refined crystal structure model in the ferroelectric phase is shown in Fig. 3(b), and crystal data, structure parameters, and bond lengths are summarized, respectively, in Tables S1–S3 of the Supplemental Material [21]. The relationship of crystallographic axes between the paraelectric and ferroelectric phases is illustrated in Figs. S4(c) and S4(d), where the two sets of crystallographic axes (a_h, b_h, c_h) and (a_m, b_m, c_m) are for the hexagonal and monoclinic systems, respectively. As shown in Fig. 3(b), we adopted the split-atom model at two Tm sites. In this case, the split-atom model denotes that large atomic displacement almost along the c_h axis and plural stable sites for Tm. Figure 3(c) shows the [100]-zone HAADF-STEM image. The brightest dots and less bright dots correspond to Tm and Fe atomic columns, respectively. We clearly observed that the Fe double layer is sandwiched in between two single layers of Tm. The bright dots corresponding to Tm ions show an ellipsoidal shape elongated along the c_h axis in contrast to spherical shape images for Fe ions. This suggests that Tm ions manifest the structural fluctuation from the average position along the c_h axis, which is compatible with the split-atom model in the structure analysis by XRD. This result is completely consistent with the refined crystal structure model. $TmFe_2O_4$ exhibits characteristic displacements of Tm ions and structural distortions. We should note that the present structure refinement is incomplete, because we approximately dealt with the superstructure diffuse streaks as diffraction spots (Figs. S5 and S6). However, the structural model is consistent with the other experimental results, especially piezoelectricity, qualitatively, as shown below.

To confirm the charge ordering model, we estimated the charges of four independent Fe sites based on the bond valence sum. These sites show a little charge disproportionation as $2.5+\delta$ and $2.5-\delta$. The observed charge ordering pattern is the same as that reported by Ikeda *et al.* [12] in a broad sense [Fig. 4(a)]. Figure 4(b) illustrates the weighted average model, that is the sum of multiplication of occupancy and coordination of split sites, for the positions of cations. The weighted average positions of two independent Tm^{3+} ions, of which the Wyckoff positions are 2*a* and 4*b*, are drawn. Actually, Tm^{3+} ions exhibit down-up-up displacements as indicated by the black and red arrows in Tm^{3+} ions denoted by the green and orange circles. The difference along the c_h axis between the green and orange circles, of which positions are 2*a* and 4*b*, respectively, is 0.0680 Å. It should be noted that the ordered displacements of Tm ions coincide with the arrangements of $Fe^{2.5-\delta}$ and $Fe^{2.5+\delta}$ ions. We believe that the charge ordering of Fe ions is accompanied with atomic displacements of Tm ions cooperatively. The charge ordering and Tm displacement in our experimental crystal structure model are qualitatively in good agreement with those deduced from the first-principles calculations for a polar state by Mundy *et al.* [49]. We also performed first-principles calculations based on density-functional theory within the generalized gradient approximation. The result suggests that a polar state with Cm symmetry is the most stable for $TmFe_2O_4$, although the difference in energy between polar and antipolar states is rather small (Figs. S7 and S8). Furthermore, we calculated the spontaneous polarization induced by the ionic displacements (P_{ion}) and charge ordering (P_{ele}) parallel to the c_h axis by the point charge model. P_{ion} is due to the ionic displacement from the position of the centrosymmetric structure. As seen in Fig. 4(b), displacements of Tm ions along the c_h direction break the centrosymmetry, leading to a conventional polar structure. The present result, therefore, suggests that rare-earth ions in RFe_2O_4 play an important role for spontaneous polarization. On the other hand, P_{ele} is calculated from the electric dipole formed by the charge of Fe ions, that is an electronic ferroelectricity. P_{ion} and P_{ele} are estimated as 10.5 and 3.5 $\mu C/cm^2$, respectively. Although these values are not strictly quantitative due to the assumption of the point charge model, these results indicate that the main contributions to the spontaneous polarization are both atomic

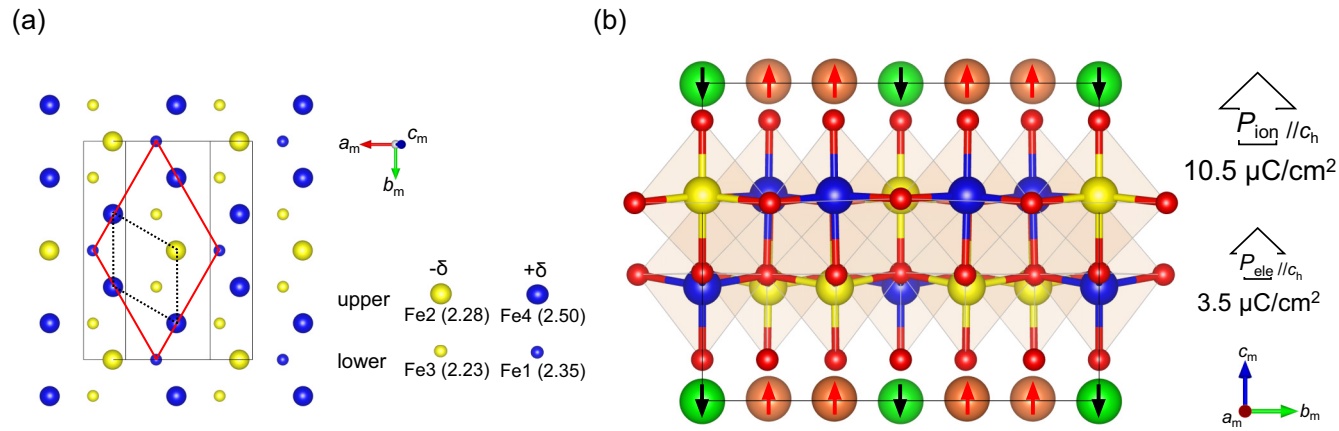

FIG. 4. Origin of the charge order-driven ferroelectricity in $TmFe_2O_4$. (a) Charge ordering model of $TmFe_2O_4$. Yellow and blue circles denote electric charges of $2.5-\delta$ and $2.5+\delta$, respectively. Black dotted line shows a prototype of trigonal structure. Red line indicates a charge ordered unit cell, which is similar to the model proposed by Ikeda *et al.* [12]. (b)Weighted average model of Tm ion. Red and black arrows represent displacement directions.

displacements of Tm^{3+} ions and the charge ordering among Fe ions. We consider that the ordered arrangement of Fe^{2+} and Fe^{3+}, i.e., the charge ordering, causes the zigzag structure of Tm^{3+} displacement through the electrostatic interaction between Tm^{3+} and Fe ions with different valence states, leading to the spontaneous polarization.

IV. CONCLUSION

In summary, we focused on $TmFe_2O_4$, one of the compounds thought to be an electronic dielectric, in the present study. We experimentally demonstrated that the compound is ferroelectric as well as piezoelectric at room temperature. The SS-PFM revealed that spontaneous polarization of $TmFe_2O_4$ is present and that these spontaneous polarizations can be reversed by applying electric fields. The piezoelectric coefficient d_{33} was evaluated to be 64 pm V^{-1} by using laser interferometry. Moreover, we found a phase transition between ferroelectric and conductive states induced by an electric field due to the conversion between charge ordered and disordered states of Fe ions. A detailed structural analysis based on XRD and HAADF-STEM indicates that an ordered displacement of Tm^{3+} ions accompanying charge ordering among Fe ions takes place at room temperature. We propose a model of electronic dielectric that the charge ordering among Fe ions and the displacement of Tm^{3+} ions lead to the ferroelectricity and piezoelectricity of $TmFe_2O_4$.

ACKNOWLEDGMENTS

The present authors would like to thank aixACCT Systems GmbH, Germany for the measurements of dielectric properties using laser interferometry and the LCR meter. The authors would like to thank Prof. Taka-hisa Arima, University of Tokyo for discussion about the dielectric properties. This work was supported by JSPS KAKENHI Grants No. JP17H01320, No. JP19KK0124, No. JP21K03431, No. JP21K04641, and No. JP21H04619 and the Collaborative Research Project of Materials and Structures Laboratory, Tokyo Institute of Technology. Part of this work was carried out under the Interdisciplinary Research Project Program of Nagoya Institute of Technology.

[1] E. Bousquet, M. Dawber, N. Stucki, C. Lichtensteiger, P. Hermet, S. Gariglio, J. M. Triscone, and P. Ghosez, Improper ferroelectricity in perovskite oxide artificial superlattices, Nature (London) **452**, 732 (2008).

[2] N. A. Benedek and C. J. Fennie, Hybrid Improper Ferroelectricity: A Mechanism for Controllable Polarization-Magnetization Coupling, Phys. Rev. Lett. **106**, 107204 (2011).

[3] N. A. Benedek, A. T. Mulder, and C. J. Fennie, Polar octahedral rotations: A path to new multifunctional materials, J. Solid State Chem. **195**, 11 (2012).

[4] J. M. Rondinelli and C. J. Fennie, Octahedral rotation-induced ferroelectricity in cation ordered perovskites, Adv. Mater. **24**, 1961 (2012).

[5] A. T. Mulder, N. A. Benedek, J. M. Rondinelli, and C. J. Fennie, Turning ABO_3 antiferroelectrics into ferroelectrics: Design rules for practical rotation-driven ferroelectricity in double perovskites and $A_3B_2O_7$ Ruddlesden-Popper compounds, Adv. Funct. Mater. **23**, 4810 (2013).

[6] P. V. Balachandran, D. Puggioni, and J. M. Rondinelli, Crystal-Chemistry Guidelines for noncentrosymmetric A_2BO_4 ruddlesden−popper oxides, Inorg. Chem. **53**, 336 (2014).

[7] M. S. Senn, A. Bombardi, C. A. Murray, C. Vecchini, A. Scherillo, X. Luo, and S. W. Cheong, Negative Thermal Expansion in Hybrid Improper Ferroelectric Ruddlesden-Popper Perovskites by Symmetry Trapping, Phys. Rev. Lett. **114**, 035701 (2015).

[8] M. J. Pitcher, P. Mandal, M. S. Dyer, J. Alaria, P. Borisov, H. Niu, J. B. Claridge, and M. J. Rosseinsky, Tilt engineering of spontaneous polarization and magnetization above 300 K in a bulk layered perovskite, Science **347**, 420 (2015).

[9] S. Yoshida, K. Fujita, H. Akamatsu, O. Hernandez, A. S. Gupta, F. G. Brown, H. Padmanabhan, A. S. Gibbs, T. Kuge, R. Tsuji, S. Murai, J. M. Rondinelli, V. Gopalan, and K. Tanaka, Ferroelectric $Sr_3Zr_2O_7$: Competition between hybrid improper ferroelectric and antiferroelectric mechanisms, Adv. Funct. Mater. **28**, 1801856 (2018).

[10] Y. Wang, F.-T. Huang, X. Luo, B. Gao, and S.-W. Cheong, The first room-temperature ferroelectric Sn insulator and its polarization switching kinetics, Adv. Mater. **29**, 1601288 (2017).

[11] S. Yoshida, H. Akamatsu, R. Tsuji, O. Hernandez, H. Padmanabhan, A. S. Gupta, A. S. Gibbs, K. Mibu, S. Murai, J. M. Rondinelli, V. Gopalan, K. Tanaka, and K. Fujita, Hybrid improper ferroelectricity in $(Sr, Ca)_3 Sn_2O_7$ and beyond: Universal relationship between ferroelectric transition temperature and tolerance factor in $n = 2$ Ruddlesden–Popper phases, J. Am. Chem. Soc. **140**, 15690 (2018).

[12] N. Ikeda, H. Ohsumi, and K. Ohwada, Ferroelectricity from iron valence ordering in the charge-frustrated system $LuFe_2O_4$, Nature (London) **436**, 1136 (2005).

[13] J. de Groot, T. Mueller, R. A. Rosenberg, D. J. Keavney, Z. Islam, J.-W. Kim, and M. Angst, Charge Order in $LuFe_2O_4$: An Unlikely Route to Ferroelectricity, Phys. Rev Lett. **108**, 187601 (2012).

[14] A. Ruff, S. Krohns, F. Schrettle, V. Tsurkan, P. Lunkenheimer, and A. Loidl, Absence of polar order in $LuFe_2O_4$, Eur. Phys. J. B **85**, 290 (2012).

[15] J. Y. Park, J. H. Park, Y. K. Jeong, and H. M. Jang, Dynamic magnetoelectric coupling in "electronic ferroelectric" $LuFe_2O_4$, Appl. Phys. Lett. **91**, 152903 (2007).

[16] D. S. F. Viana, R. A. M. Gotardo, L. F. Cótica, I. A. Santos, M. Olzon-Dionysio, S. D. Souza, D. Garcia, J. A. Eiras, and A. A. Coelho, Ferroic investigations in $LuFe_2O_4$ multiferroic ceramics, J. Appl. Phys. **110**, 034108 (2011).

[17] S. Lafuerza, J. García, G. Subías, J. Blasco, K. Conder, and E. Pomjakushina, Intrinsic electrical properties of $LuFe_2O_4$, Phys. Rev. B **88**, 085130 (2013).

[18] M. Angst, Ferroelectricity from iron valence ordering in rare earth ferrites? Phys. Status Solidi RRL **7**, 383 (2013).

[19] N. Ikeda, T. Nagata, J. Kano, and S. Mori, Present status of the experimental aspect of RFe_2O_4 study, J. Phys.: Condens. Matter **27**, 053201 (2015).

[20] K. Yang, J. H. Kim, S. H. Lee, S.-W. Cheong, and Y. H. Jeong, Charge ordering, ferroelectric, and magnetic domains in $LuFe_2O_4$ observed by scanning probe microscopy, Appl. Phys. Lett. **106**, 152902 (2015).

[21] See Supplemental Material at http://link.aps.org/supplemental/10.1103/PhysRevB.108.014105 for method of theoretical calculations, which include Refs. [13,22–35,49]

[22] J. P. Perdew, A. Ruzsinszky, G. I. Csonka, O. A. Vydrov, G. E. Scuseria, L. A. Constantin, X. Zhou, and K. Burke, Restoring the Density-Gradient Expansion for Exchange in Solids and Surfaces, Phys. Rev. Lett. **100**, 136406 (2008).

[23] P. E. Blöchl, Projector augmented-wave method, Phys. Rev. B **50**, 17953 (1994).

[24] G. Kresse and D. Joubert, From ultrasoft pseudopotentials to the projector augmented-wave method, Phys. Rev. B **59**, 1758 (1999).

[25] G. Kresse and J. Hafner, *Ab initio* molecular dynamics for liquid metals, Phys. Rev. B **47**, 558(R) (1993).

[26] G. Kresse and J. Hafner, *Ab initio* molecular-dynamics simulation of the liquid-metal–amorphous-semiconductor transition in germanium, Phys. Rev. B **49**, 14251 (1994).

[27] G. Kresse and J. Furthmüller, Efficiency of *ab-initio* total energy calculations for metals and semiconductors using a plane-wave basis set, Comput. Mater. Sci. **6**, 15 (1996).

[28] G. Kresse and J. Furthmüller, Efficient iterative schemes for *ab initio* total-energy calculations using a plane-wave basis set, Phys. Rev. B **54**, 11169 (1996).

[29] S. L. Dudarev, G. A. Botton, S. Y. Savrasov, C. J. Humphreys, and A. P. Sutton, Electron-energy-loss spectra and the structural stability of nickel oxide: An LSDA+U study, Phys. Rev. B **57**, 1505 (1998).

[30] Y. Yamada, S. Nohdo, N. Ikeda, Incommensurate charge ordering in charge-frustrated $LuFe_2O_4$ system, J. Phys. Soc. Jpn **66**, 3733 (1997).

[31] H. Z. Jin, J. Zhu, S. Miao, X. W. Zhang, and Z. Y. Cheng, Ordered domains and polar clusters in lead magnesium niobite $Pb(Mg_{1/3}Nb_{2/3})O_3$, J. Appl. Phys. **89**, 5048 (2001).

[32] B. F. Buxton, J. A. Eades, J. W. Steeds, and G. M. Rackham, The symmetry of electron diffraction zone axis patterns, Philos. Trans. R. Soc. A **281**, 171 (1976).

[33] M. Tanaka, R. Saito, and H. Sekii, Point-group determination by convergent-beam electron diffraction, Acta Crystallogr. Sect. A **39**, 357 (1983).

[34] K. Tsuda and M. Tanaka, Nanometer-scale local structural study of the paraelectric cubic phase of $KNbO_3$ by convergent-beam electron diffraction, Jpn. J. Appl. Phys. **56**, 10PB09 (2017).

[35] K. Parlinski, V. Heine, and E. K. H. Salje, Origin of tweed texture in the simulation of a cuprate superconductor, J. Phys.: Condens. Matter **5**, 497 (1993).

[36] S. Konishi, K. Oka, H. Eisaki, K. Tanaka, and T. Arima, Growth of single-crystalline $RFe_2O_{4-\delta}$ (R = Y, Tm, Yb) by the floating zone melting method in a mixture of N_2, H_2, and CO_2 gases and magnetic properties of the compounds, Cryst. Growth Des. **19**, 5498 (2019).

[37] Y. Kim, S. Konishi, M. Okada, M. Komabuchi, D. Urushihara, T. Asaka, and K. Tanaka, Spin glass transition of single-crystalline $TmFe_2O_{4-\delta}$, J. Phys.: Condens. Matter **32**, 405801 (2020).

[38] S. Jesse, H. N. Lee, and S. V. Kalinina, Quantitative mapping of switching behavior in piezoresponse force microscopy, Rev. Sci. Instrum. **77**, 073702 (2006).

[39] APEX3, SAINT, and SADABS (Bruker AXS Inc., Madison, (2015).

[40] L. Palatinus and G. Chapuis, SUPERFLIP - a computer program for the solution of crystal structures by charge flipping in arbitrary dimensions, J. Appl. Crystallogr. **40**, 786 (2007).

[41] V. Petricek, M. Dusek, and L. Palatinus, Crystallographic computing system JANA2006: General features, Z. Kristallogr. Cryst. Mater. **229**, 345 (2014).

[42] K. Momma and F. Izumi, VESTA 3 for three-dimensional visualization of crystal, volumetric and morphology data, J. Appl. Crystallogr. **44**, 1272 (2011).

[43] DeConvHAADF is commercially available from HREM Research, Inc. Available from www.hremresearch.com.

[44] R. K. Vasudevan, N. Balke, P. Maksymovych, S. Jesse, and S. V. Kalinin, Ferroelectric or non-ferroelectric: Why so many materials exhibit "ferroelectricity" on the nanoscale, Appl. Phys. Rev. **4**, 021302 (2017).

[45] L. J. Zeng, H. X. Yang, Y. Zhang, H. F. Tian, C. Ma, Y. B. Qin, Y. G. Zhao, and J. Q. Li, Nonlinear current-voltage behavior and electrically driven phase transition in charge-frustrated $LuFe_2O_4$, Europhys. Lett. **84**, 57011 (2008).

[46] K. Fujiwara, T. Hori, and H. Tanaka, Electric-field breakdown of the insulating charge-ordered state in $LuFe_2O_4$ thin films, J. Phys. D: Appl. Phys. **46**, 155108 (2013).

[47] C. Li, X. Zhang, Z. Cheng, and Y. Sun, Electric field induced phase transition in charge-ordered $LuFe_2O_4$, Appl. Phys. Lett. **93**, 152103 (2008).

[48] S. Cao, J. Li, H. F. Tian, Y. B. Qin, L. J. Zeng, H. X. Yang, and J. Q. Li, Nonlinear transport properties and Joule heating effect in charge ordered $LuFe_2O_4$, Appl. Phys. Lett. **98**, 102102 (2011).

[49] J. A. Mundy, C. M. Brooks, M. E. Holtz, J. A. Moyer, H. Das, A. F. Rébola, J. T. Heron, J. D. Clarkson, S. M. Disseler, Z. Liu, A. Farhan, R. Held, R. Hovden, E. Padgett, Q. Mao, H. Paik, R. Misra, L. F. Kourkoutis, E. Arenholz, A. Scholl *et al.*, Atomically engineered ferroic layers yield a room-temperature magnetoelectric multiferroic, Nature (London) **537**, 523 (2016).